Electronic Supplementary Information

for

Facile preparation of a cobalt diamine diketonate adduct as a potential vapor phase precursor for Co_3O_4 films

Max Klotzsche,[a] Davide Barreca,[b] Lorenzo Bigiani,[a] Roberta Seraglia,[b] Alberto Gasparotto,[a] Laura Vanin,[a] Christian Jandl,[c] Alexander Pöthig,[c] Marco Roverso,[a] Sara Bogialli,[a] Gloria Tabacchi,*[d] Ettore Fois,[d] Emanuela Callone,[e] Sandra Dirè[e] and Chiara Maccato[a]*

[a] Department of Chemical Sciences -Padova University and INSTM, Via Marzolo 1, 35131 Padova, Italy.

[b] CNR-ICMATE and INSTM - Department of Chemical Sciences - Padova University, Via Marzolo 1, 35131 Padova, Italy.

[c] Catalysis Research Center & Department of Chemistry - Technische Universität München, Lichtenbergstr. 4, 85747 Garching, Germany.

[d] Department of Science and High Technology - Insubria University and INSTM, Via Valleggio 11, 22100 Como, Italy.

[e] "Klaus Müller" Magnetic Resonance Laboratory, Department of Industrial Engineering - Trento University, Via Sommarive 9, 38123 Trento, Italy.

*Corresponding authors. E-mail: davide.barreca@unipd.it (D.B.); gloria.tabacchi@uninsubria.it (G.T.)

Table of Contents

§ S1. Structural characterization

§ S1.1 Experimental

The structural characterization of $Co(tfa)_2$•TMEDA (tfa = 1,1,1-trifluoro-2,4-pentanedionate; TMEDA = *N*,*N*,*N'*,*N'*-tetramethylethylenediamine) was carried out on single crystals coated with perfluorinated ether, fixed on a kapton micro-sampler and frozen under a cold nitrogen stream. The initial lattice parameters were determined by a matrix scan. Lorentz and polarization effects, scan speed, and background corrections on the reflections were performed using *SAINT*,[1] whereas absorption correction, including odd and even-ordered spherical harmonics, was carried out using *SADABS*.[2] The assignment of space group was based on systematic absences and structure refinement. Methyl hydrogen atoms were refined as part of rigid rotating groups, with a C–H distance of 0.98 Å and $U_{iso(H)} = 1.5 \cdot U_{eq(C)}$. The other H atoms were located in calculated positions and refined using a riding model (methylene and conjugated C–H distances = 0.99 Å and 0.95 Å, respectively; other C–H distances = 1.00 Å; all with $U_{iso(H)} = 1.2 \cdot U_{eq(C)}$). Non-hydrogen atoms were refined with anisotropic displacement parameters. Full-matrix least-squares refinements were performed by the minimization of $[\Sigma w(F_o^2 - F_c^2)^2]$ with the SHELXL weighting scheme.[3] Neutral atom scattering factors and anomalous dispersion corrections for non-hydrogen atoms were taken from *International Tables for Crystallography*.[4] A split layer refinement was adopted for disordered groups using, if necessary, additional restraints on geometries and anisotropic displacement parameters. PLATON[5] was used to generate images of the crystal structure. Supplementary crystallographic data for this paper are contained in CCDC 2082367. These data are provided free of charge by the Cambridge Crystallographic Data Centre.

Crystal data	
$C_{16}H_{24}O_4N_2F_6Co$	M_r = 481.30
D_x = 1.528 Mg m^{-3}	Monoclinic, *C*2/*c*
Hall symbol: -C 2yc	Mo *K*α radiation, λ = 0.71073 Å
a = 8.8629 (6) Å	Cell parameters from 9949 reflections
b = 13.2939 (9) Å	θ = 2.3–26.7°
c = 17.7715 (12) Å	μ = 0.90 mm^{-1}
β = 91.719 (2)°	*T* = 100 K
V = 2092.9 (2) Å^3	Fragment, orange
Z = 4; *F*(000) = 988	0.30 × 0.12 × 0.10 mm
Data collection	Bruker Photon CMOS diffractometer
32587 measured reflections	2135 independent reflections
Radiation source: IMS microsource	1940 reflections with $I > 2\sigma(I)$
Helios optic monochromator	R_{int} = 0.101
Detector resolution: 16 pixels mm^{-1}	θ_{max} = 26.4°, θ_{min} = 2.3°
phi– and ω–rotation scans	*h* = −11 10
Absorption correction: multi-scan *SADABS* 2016/2, Bruker	*k* = −16 16
T_{min} = 0.700, T_{max} = 0.745	*l* = −22 22
Refinement	Primary atom site location: iterative
Refinement on F^2	Secondary atom site location: difference Fourier map
Least-squares matrix: full	Hydrogen site location: inferred from neighboring sites
$R[F^2 > 2\sigma(F^2)]$ = 0.029	H-atom parameters constrained
$wR(F^2)$ = 0.074	W = 1/[Σ^2(*F*O^2) + (0.0294*P*)^2 + 2.6364*P*] where *P* = (*F*O^2 + 2*F*C^2)/3
S = 1.06	$(\Delta/\sigma)_{max} < 0.001$
2135 reflections	$\Delta\rho_{max}$ = 0.30 e Å^{-3}
135 parameters	$\Delta\rho_{min}$ = −0.43 e Å^{-3}
0 restraints	Extinction correction: none
0 constraints	Extinction coefficient: -

Table S1. Crystallographic data and structure refinement for Co(tfa)$_2$•TMEDA.

§ S2. NMR spectroscopy characterization

The spectrum of $Co(tfa)_2$•TMEDA recorded in $CDCl_3$ (Fig. S1) shows that the signals are spread on a slightly narrow chemical shift range.

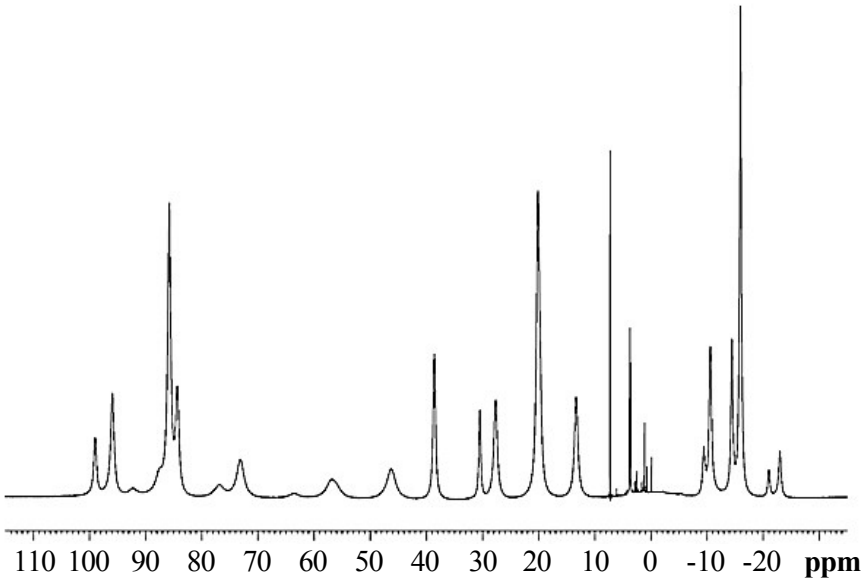

Figure S1. ^{1}H NMR spectrum of $Co(tfa)_2$•TMEDA in $CDCl_3$ (solvent signal at 7.24 ppm, the other small sharp peaks in the 10-0 ppm region belongs to impurities).

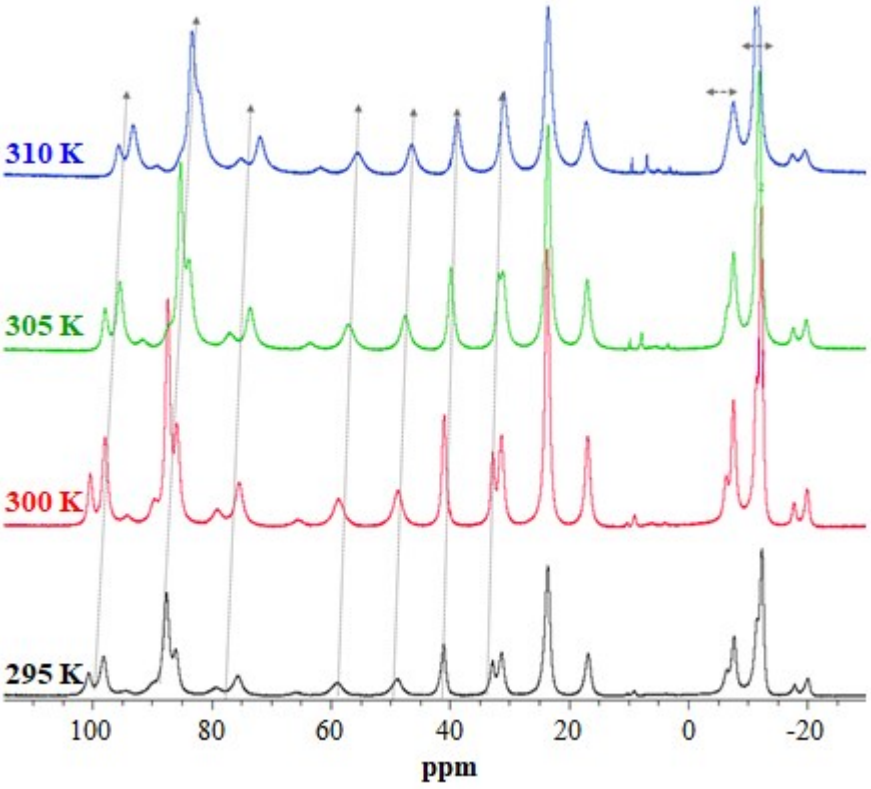

Figure S2. ^{1}H variable temperature NMR spectra of $Co(tfa)_2$•TMEDA.

Most of the analytical work has been done on the $CDCl_3$ solution. A small range of different temperatures has been also tested to verify the trend of the Curie plot (the plots of chemical shift *vs*. the reciprocal absolute temperature; see Fig. S2). It can be observed that the more downfield shifted signals move rapidly to lower frequencies with increasing temperature, theoretically converging to the diamagnetic chemical shift range, in agreement with the approximate Curie Law.[6] Since the temperature interval is very small and close to room temperature, the phenomenon suggests only that they are closer or more sensitive to the metal center paramagnetism.

For solid-state analysis, a cross polarization/magic angle spinning (CPMAS) dual band probe was used for ^{13}C cross polarization experiment ($\pi/2$ 3.5 μs, recycle delay 3 s, contact time 3 s, and 10 k scans). The powdered sample was packed in 4 mm zirconia rotors, spun at 8 or 11 kHz under air at room temperature.

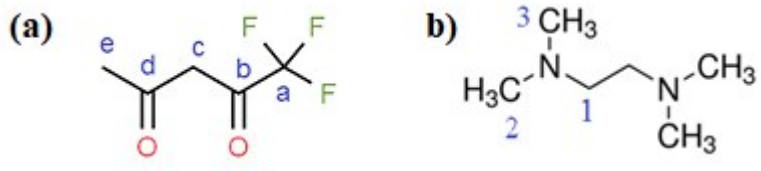

Scheme S1. Molecular structure of the (a) tfa and (b) TMEDA ligands and labelling of carbon atoms.

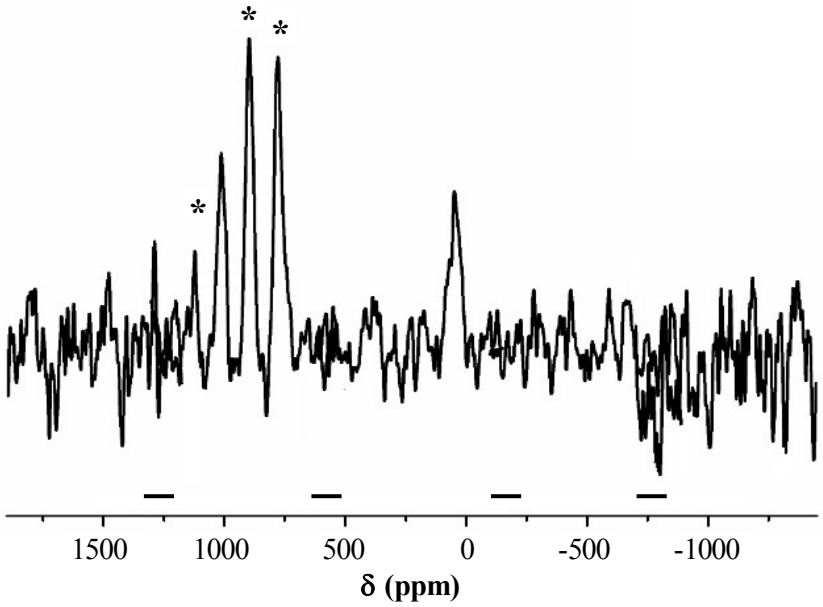

Figure S3. ^{13}C CPMAS spectrum as a sum of 5 spectra with 800 ppm of spectral width, spinning sidebands are marked with *, overlay regions are indicated with –.

In order to prove the complex stability, the sample has been analyzed by solid-state NMR. Fig. S3 displays the ^{13}C CPMAS spectrum of the Co compound, in which two main resonances, broadened due to the metal center complexation, are clearly visible. The first resonance falls in the typical aliphatic region. The asymmetric line shape indicated that it is composed by at least two overlapped peaks centered

at ≈ 69 and 40 ppm. Using the labelling proposed in Scheme S1, the former component is attributable to C-H moieties (**1, c**) of both TMEDA and tfa, whereas the latter could be assigned to methyl groups (e**, 2, 3**) of both TMEDA and tfa. It can be argued that, in agreement with the liquid NMR results, there is a low and noisy signal at ≈400 ppm attributable to the CF_3 groups (**a**), due to the terminal F-C coupling broadening. The second clear resonance, centered at 1014 ppm and with an asymmetric sideband pattern, refers to the C=O groups (**b, d**) complexing the metal center. The interaction is clearly represented by both the wide downfield shift of the C=O peak, normally detected at 194 ppm, and the sideband pattern, indicating a wide chemical shift anisotropy of the peak. The correct position of the carbonyl peak is obtained through the comparison of two spectra collected at two different spinning speed, as shown in Fig. S4.

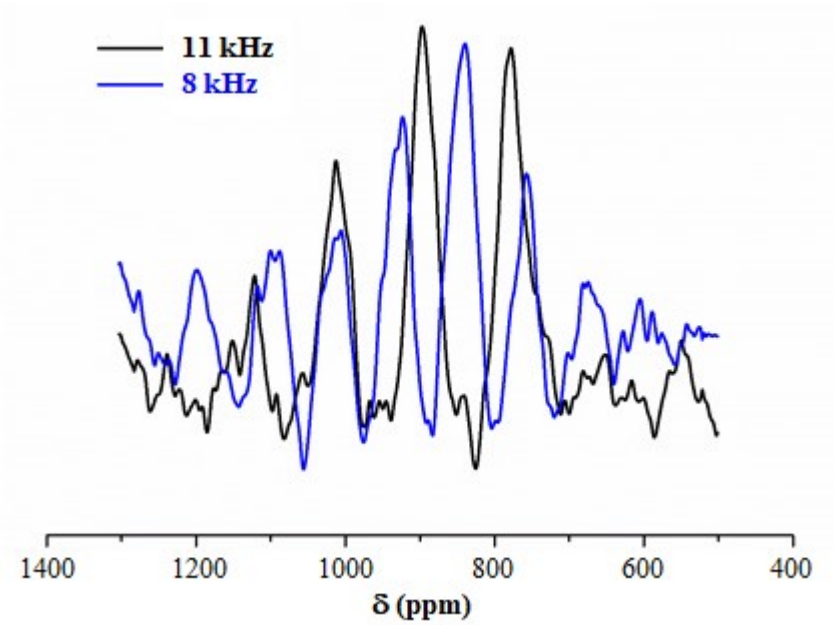

Figure S4. ^{13}C CPMAS spectra of $Co(tfa)_2$•TMEDA in the C=O range recorded at two different spinning speeds.

§ S3. IR spectroscopy characterization

IR spectra were acquired in transmittance mode on KBr pellets by a Thermo-Nicolet Nexus 860 spectrometer (resolution = 4 cm^{-1}). Experimental IR data were compared with theoretical vibrational frequencies computed on $Co(tfa)_2$•TMEDA optimized geometry (see also § S5), which had all positive frequencies.

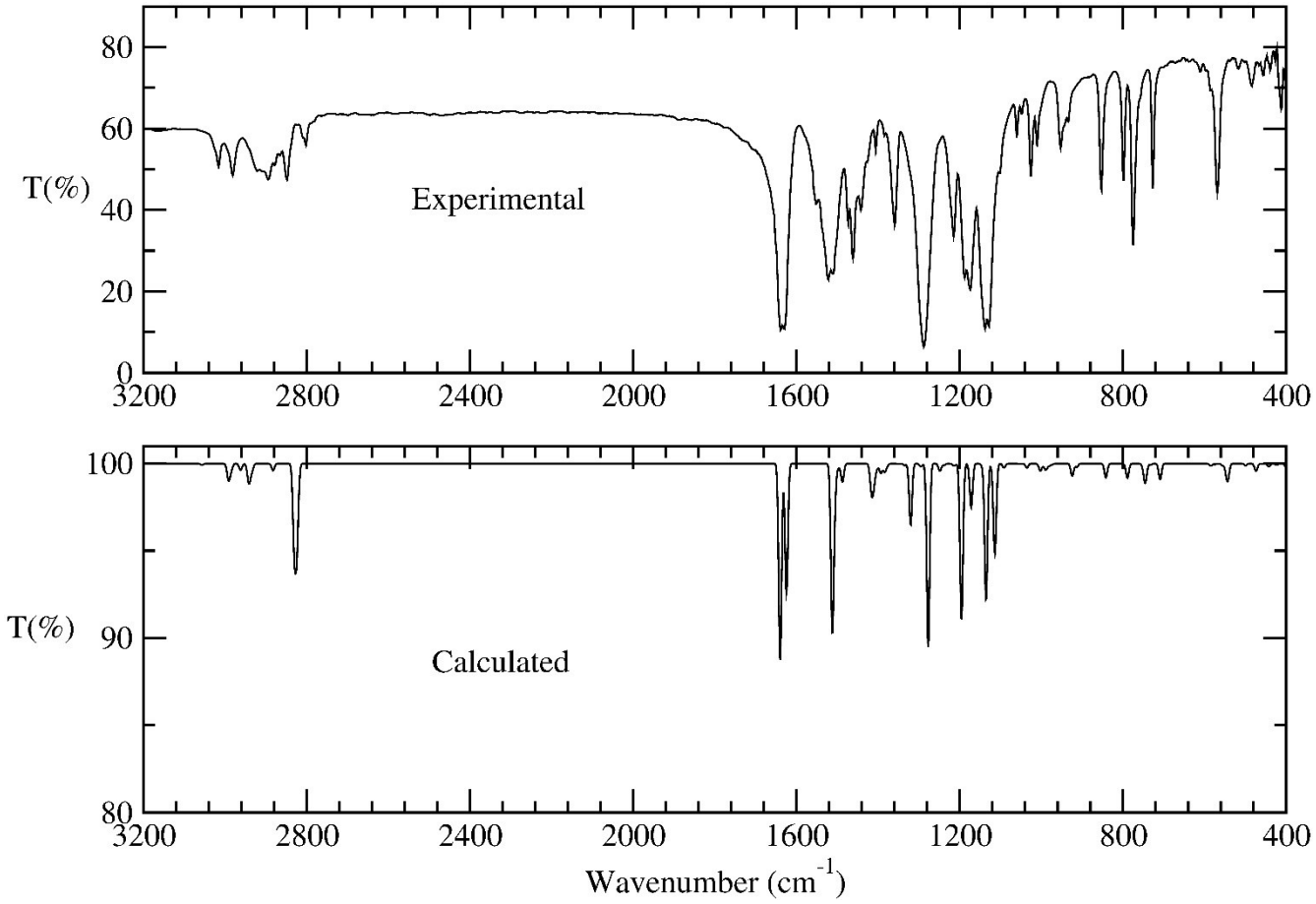

Figure S5. Experimental and calculated IR spectra of $Co(tfa)_2$•TMEDA. A scaling factor of 0.952 was applied to the computed vibrational frequencies.[7, 8]

The experimental and simulated IR spectra of $Co(tfa)_2$•TMEDA are displayed in Fig. S5. As it can be seen, the agreement between experimental and theoretical spectra is satisfactory. As a general remark, the spectral features closely resemble the ones pertaining to $Co(hfa)_2$•TMEDA (hfa = 1,1,1,5,5,5-hexafluoro-2,4-pentanedionate)[9, 10] and are similar to those of previously reported $M(hfa)_2$•TMEDA compounds (with M = Fe, Mn, Cu, Zn),[11-14] due to the analogous coordination sphere of the metal centers. A detailed assignment of the bands is reported in Table S2 (wavenumbers refer to computed values; intensities are denoted as vs = very strong; s = strong; m = medium; w = weak; vw = very weak).

$\tilde{\nu}$ (cm^{-1})	$\tilde{\nu}_s$ (cm^{-1})	$\tilde{\nu}_{exp}$(cm^{-1})	**Assignment**
3210 (vw)	3056	3166	Stretching of tfa central C-H
3143-2960 (m,w)	2992-2818	3015-2848	tfa and TMEDA –CH_3/–CH_2 stretching
2973-2967 (m,w)	2830-2825	2811-2802	TMEDA –CH_3 /–CH_2 stretching
1723 (vs)	1640	1640	Stretching C=O in-phase
1707 (vs)	1625	1627	Stretching C=O out-of-phase
1589-1563 (vs)	1513-1488	1552-1459	Stretching C=C-C tfa
1489-1203 (m)	1418-1145	1474-1200	Wagging, rocking, twisting, scissoring of –CH_3 / –CH_2
1387 (s)	1320	1359	Scissoring –CH_3 tfa
1342,1341 (vs)	1278,1277	1289	Stretching C–CF_3/C=C + bending –CH tfa + scissor –CH_3 tfa
1257,1255 (s)	1197,1195	1215	Stretching C-F + bending –CH tfa + stretching C–CF_3
1193,1192 (s)	1136, 1135	1188, 1175	Stretching C-F + bending –CH tfa + stretching C–CF_3
1177-1170 (vs)	1121-1114	1137, 1128	In-plane bending –CH + stretching C-F, C-C=C, C–CF_3 tfa
1146 (m)	1091	1101	Twisting –CH_3/–CH_2 TMEDA + C-N-C asymm. stretching
1088 (m)	1036	1060	Stretching C-C TMEDA
1053, 1039 (m)	1002,989	1047	Stretching C-N/C-CH_3 + bending N-C-C TMEDA
1031-1023 (w)	982-974	1025, 1006	In-plane and out-of-plane bending modes tfa
971 (m)	924	953-932	Collective bending N-C-C-N TMEDA
884 (m)	842	852	Collective bending tfa + bending C-O-Co
829 (m)	789	798	Bending C-N-Co
783 (m)	745	774	Out-of-plane bending O-C-C, C-C-H tfa
745 (m)	709	726	Stretching Co-O bonds (all) + bending O-C-C tfa
574 (m)	546	569	Bending O-Co-O
570 (m)	543	517	Bending Co-O-C
498 (m)	474	484	Stretching Co-O1, Co-O1a, Co-N1, Co-N1a
485 (vw)	462	466	Symmetric stretching Co-O1, Co-O1a
465 (w)	443	456	Asymmetric stretching Co-N1, Co-N1a
444 (w)	423	439	Frustrated bending N1-Co-N1a
422 (vw)	402	425	Frustrated bending O-Co-O
418 (w)	398	411	Asymmetric stretch Co-O2, Co-O2a
398 (w)	378		Frustrated bending N1-Co-N1a
339, 337 (vw)	322, 321		Stretching Co-O2, Co-O2a
277, 257 (w)	264, 245		Vibration of Co in the O2-O2a-N1-N1a plane
260, 208 (m,w)	248, 190		Vibration of Co out of the O2-O2a-N-N1a plane
192-64 (w)	183-60		Collective stretching/bending modes of the Co octahedron

Table S2. Calculated $\tilde{\nu}$, scaled $\tilde{\nu}_s$ (scaling factor=0.952)[7, 8] and experimental $\tilde{\nu}_{exp}$ wavenumbers (uncertainty = ±4 cm^{-1}) with band assignment for IR spectra in Fig. S5. For wavenumbers < 400 cm^{-1}, only calculated values, relative to the low-energy modes of the Co environment, are reported.

§ S4. Mass spectrometry characterization

m/z (R.A., %)	Proposed assignments
365 (88.9)	$[Co(tfa)_2]^{+\bullet}$
350 (21.9)	$[Co(tfa)_2 - CH_3]^+$
296 (92.9)	$[Co(tfa)_2 - CF_3]^+$
254 (16.5)	$[Co(tfa)_2 - CF_3 - CH_2CO]^+$
226 (13.1)	$[Co(tfa)_2 - CF_3 - HCF_3]^+$
212 (87.4)	$[Co(tfa)]^+$
162 (79.3)	$[Co(tfa) - CF_2]^{+\bullet}$
116 (10.4)	$[TMEDA]^{+\bullet}$
69 (15.6)	CF_3^+
58 (100)	$[(CH_3)_2N{=}CH_2]^+$

Table S3. Main ionic species obtained by electron ionization-mass spectrometry (EI-MS) analysis of $Co(tfa)_2$•TMEDA with relative abundance (R.A., %) and proposed assignments.

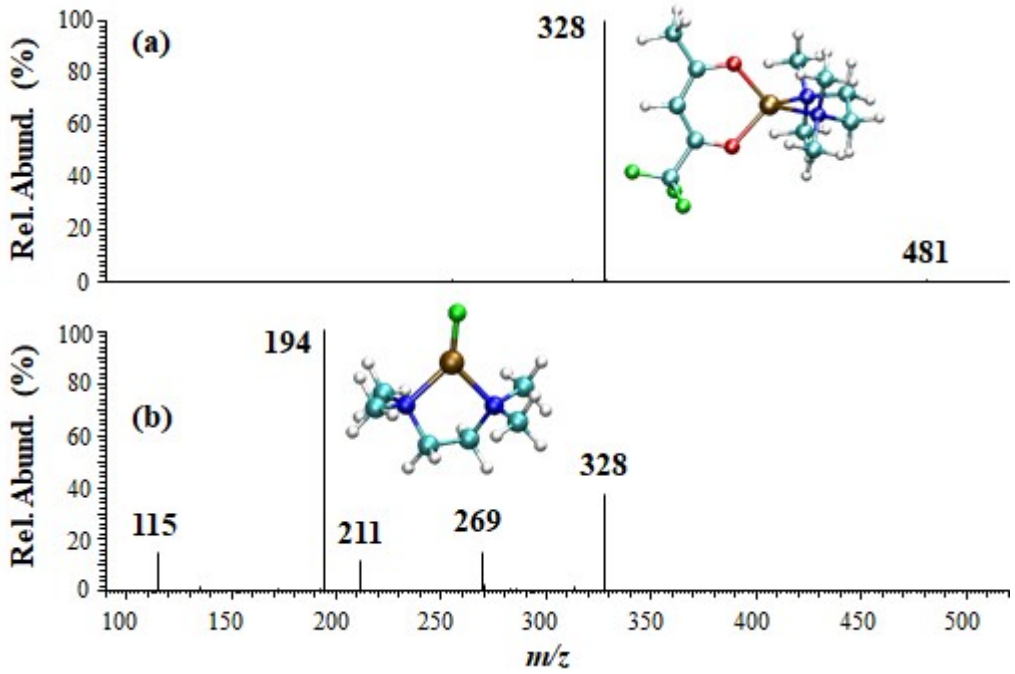

Figure S6. MS^n mass spectra obtained by ESI-MS using a three-dimensional ion trap as analyzer: (a) MS^2 of $[Co(tfa)_2$•TMEDA$]^{+\bullet}$ ion at *m/z* = 481 and (b) MS^3 of ion at *m/z* = 328, originating from $[Co(tfa)_2$•TMEDA$]^{+\bullet}$ ion. Insets: (a) M06/D95+(d,p) optimized structure of ion at *m/z* = 328, $[Co(tfa)$•TMEDA$]^+$ (spin multiplicity: quartet); (b) M06/D95+(d,p) optimized structure of ion at *m/z* = 194, $[CoF(TMEDA)]^+$ (spin multiplicity: quartet). Atom colors: Co = brown; F = green; N = blue; O = red; C = cyan; H = white.

In MS^2 experiments, the loss of tfa radical was the most favored decomposition process, leading to the ion at *m/z* = 328 (Fig. S6a), whose DFT-computed geometry is depicted in Fig. S6a, inset (for further details, see also § S5.3). The latter ionic species, in turn, yielded a more complicated collisional spectrum in comparison to the case of $[Co(hfa)TMEDA]^+$.[9] In fact, as revealed by Fig. S6b, the most favored fragmentation process leads to the formation of the abundant ion at *m/z* = 194, whose structure should be $[CoF(TMEDA)]^+$ as predicted by the DFT calculations (see Fig. S6b, inset, and Table S8). In addition, losses of TMEDA and $N(CH_3)_3$ from $[Co(tfa)TMEDA]^+$ gave rise to the signals at *m/z* = 211 and 269, respectively, whereas the ion at *m/z* = 115 corresponded to $[TMEDA-H]^+$. Such a fragmentation pathway is very different from that previously reported for $[Co(hfa)TMEDA]^+$, for which only the ion $[CoF_2•TMEDA+H]^+$ at *m/z* = 214 was revealed.[9]

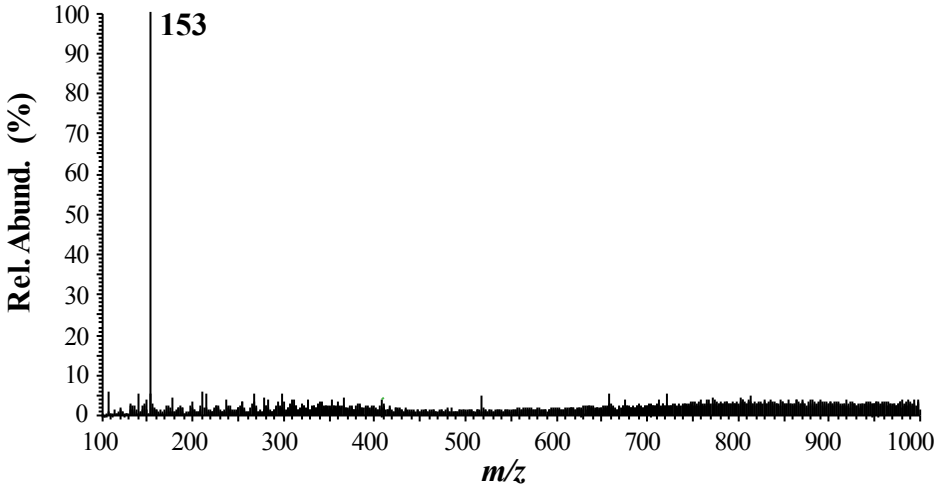

Figure S7. Electrospray ionization (ESI)-MS spectrum, in negative ion mode, of a $Co(tfa)_2$•TMEDA in acetonitrile solution.

In negative ion mode, the only peak detected in the fragmentation of $Co(tfa)_2$•TMEDA is the one at *m/z* = 153, corresponding to $[tfa]^-$ ionic species (Fig. S7). Once again, this behavior is completely different from $Co(hfa)_2$•TMEDA, that, under the same conditions, yielded $[Co(hfa)_3]^-$ and ionic species deriving from reduction products using methanol as solvent, and to the sole $[hfa]^-$ species (*m/z* = 207) if the complex was dissolved in chloroform.[9]

§ S5. Computational analysis

§ S5.1 Geometry optimization procedure and structural data

The guess geometry of the $Co(tfa)_2$•TMEDA compound was taken from the experimental XRD structure. To determine the spin state of the complex, prior to the optimization procedure, a self-consistent calculation of the magnetization of the starting model geometry was performed using Quantum Espresso (QE) code, using for Co, N, O, F, C, H the ultra-soft USPP pseudopotentials available in the QE library.[15] The electronic structure was treated with a Hubbard approach using the PBE functional[16] with D2 dispersion corrections,[17] along with a U parameter of 5.3 for Co.[18] Wavefunctions were expanded in plane waves up to a 30 Ry cutoff (240 Ry cutoff for the density). A cubic box of 20 Å length with periodic boundary conditions was used. The starting value of the magnetization in the self-consistent calculation was 1.0, corresponding to one unpaired electron. The final value of the magnetization of the $Co(tfa)_2$•TMEDA compound resulted 3.0, corresponding to a quartet spin state.

The geometry optimization of the complex was performed in the framework of hybrid DFT with Gaussian basis set and spin multiplicity = 4. In particular, the optimized structure was calculated with Gaussian 09[19] using two different hybrid functionals, M06[20] and ωB97XD[21] and by employing the D95+(d,p) basis set.[22] Significant geometrical parameters of the resulting optimized structures at both levels of theory are reported in Table S4, along with the corresponding experimental quantities. It can be seen that both functionals provide similar results and reproduce satisfactorily the geometry of the complex deduced from X-ray measurements. In particular, Co exhibits an octahedral coordination geometry, where the Co-O1/O1a distances are slightly shorter than the Co-O2/O2a ones. Also, in line with the experimental results, the Co-N bond lengths are significantly longer than the Co-O ones. A representation of the optimized geometry of $Co(tfa)_2$•TMEDA is reported in Fig. S8. All graphical representations of the computed molecular structures were created with the VMD code.[23]

	M06/D95+(d,p)	ωB97XD/D95+(d,p)	Experimental
Bond lengths (Å)			
Co-O1	2.043	2.051	2.0561(12)
Co-O1a	2.043	2.051	2.0561(12)
Co-O2	2.064	2.068	2.0736(12)
Co-O2a	2.064	2.068	2.0736(12)
Co-N1	2.197	2.221	2.1976(15)
Co-N1a	2.197	2.221	2.1976(15)
O1-C5	1.261	1.261	1.2648(12)
O2-C7	1.256	1.257	1.2520(12)
O1a-C5a	1.261	1.261	1.2648(12)
O2a-C7a	1.256	1.257	1.2520(12)
Bond angles (°)			
O1−Co−O1a	177.5	177.9	177.94(4)
O1−Co−O2	88.0	87.5	87.55(4)
N1−Co−N1a	83.4	82.7	83.16(5)
O2-Co-O2a	90.1	91.8	93.21(5)
O2-Co-N1	93.4	92.9	92.05(5)
O1- Co-N1	93.5	93.6	94.22(5)

Table S4. Geometrical data calculated for $Co(tfa)_2$•TMEDA at the levels of theory M06/D95+(d,p) and ωB97XD/D95+(d,p). Experimental data included for comparison. Atom labels as in Fig. S8. Co pseudopotential/basis set of Ref. [24].

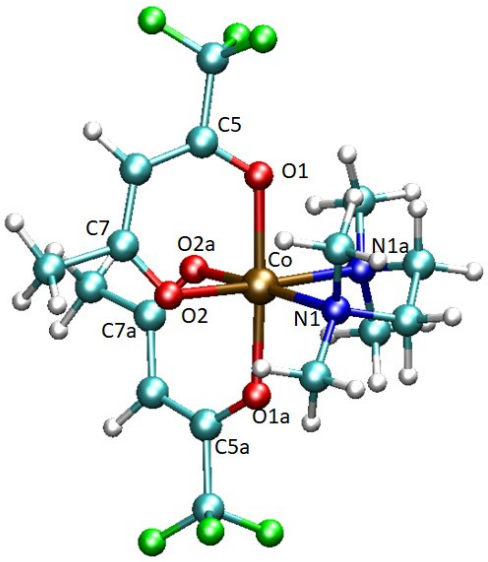

Figure S8. Optimized structure of $Co(tfa)_2$•TMEDA at the M06/D95+(d,p) level of theory. Atom colors: Co, brown; F, green; O, red; N, blue; C, cyan; H, white.

§ S5.2. Electronic structure analysis

	Total Charge	***α* spin**	***β* spin**
Co	+1.685	−0.651	+2.336
N1	−0.754	−0.382	−0.372
N1a	−0.754	−0.382	−0.372
O1	−1.042	−0.648	−0.394
O1a	−1.042	−0.648	−0.394
O2	−0.813	−0.411	−0.402
O2a	−0.813	−0.411	−0.402
tfa	−0.903	−0.453	−0.450
TMEDA	+0.120	+0.056	+0.064

Table S5. NBO charges calculated for atoms in the Co coordination sphere and for TMEDA, tfa ligands in $Co(tfa)_2$•TMEDA. Atom labels as in Fig. S8.

Comment to Table S5. The Natural Bond Orbital (NBO) charge analysis[25, 26] indicates donation of an electronic charge fraction of 0.315 *e* from the ligands to the Co(II) center. The six atoms bonded to Co bear a negative fractional charge, which is greater for the O atoms than for the N ones. Charge donation also occurs from ligand atoms not directly bonded to the metal center. By considering that the total charges of free tfa and TMEDA ligands are -1 and 0, respectively, each tfa donates to Co 0.097 *e*, while the fractional charge donated to Co by TMEDA is 0.120 *e*. This result indicates that, in this complex, the electron-donor effect of the diamine ligand towards Co is higher than that of a single diketonate ligand.

bond	$Co(tfa)_2$•TMEDA
Co–N1	0.121
Co–N1a	0.121
Co–O1	0.197
Co–O1a	0.197
Co–O2	0.192
Co–O2a	0.192

Table S6. Bond orders calculated for $Co(tfa)_2$•TMEDA.

Comment to Table S6. The bond orders represent an estimate of the relative strengths of the Co–N and Co–O interactions in the $Co(tfa)_2$•TMEDA complex. The Co-N bond order are by 37% lower than the average of the Co–O bond orders in $Co(tfa)_2$•TMEDA, indicating that the Co–N bonds are weaker than the Co–O ones.

§ S5.3. Fragmentation of the complex

The energetics corresponding to the fragmentation of the complex along the two pathways (1) and (2):

$Co(tfa)_2$•TMEDA $\rightarrow$ $Co(tfa)_2$ + TMEDA (1), loss of TMEDA

$Co(tfa)_2$•TMEDA $\rightarrow$ Co(tfa)•$TMEDA^+$ + tfa^- (2), loss of tfa^-

were computed based on the total energies of the parent complex $Co(tfa)_2$•TMEDA and the fragments formed upon the loss of TMEDA and tfa^- ligands, respectively. To calculate the pertaining fragmentation energies – denoted as ΔE_1 and ΔE_2, respectively – the geometries of all fragments were optimized at the M06/D95+(d,p) level, and the respective energies were corrected by adding the zero point energy (ZPE) (see Table S7). The data clearly show that the loss of TMEDA (pathway 1) is energetically favored over the loss of a tfa^- ligand (pathway 2), suggesting that the diamine loss might be the most likely precursor decomposition path in the gas phase.

Graphical representations of the Co(tfa)•$(TMEDA)^+$ and $Co(tfa)_2$ fragments are reported in Fig. S9a-c. Co(tfa)•$(TMEDA)^+$ exhibits two energetically close structures: whereas the most stable one is characterized by a tetrahedral coordination geometry (see Fig. S9a and Tables S7-S8), a second distorted square structure - less stable by 4.12 kcal×mol^{-1} (Table S7) - is characterized by O2-Co-N1 angle of 154.6º (Fig. S9b, Table S8). On the other hand, a single structure was found for $Co(tfa)_2$, exhibiting a distorted square geometry around the metal center (Fig. S9c), with O1-Co-O1a and O2-Co-O2a angles of 148.5° and 147.6º, respectively (Table S8). Due to Co undercoordination, Co-ligand distances in these fragments are shorter than in the parent compound (Table S8). Self-consistent calculation of the

magnetization indicated that the $Co(tfa)_2$ and $Co(tfa)•(TMEDA)^+$ structures have a multiplicity of 4, as for $Co(tfa)_2$•TMEDA.

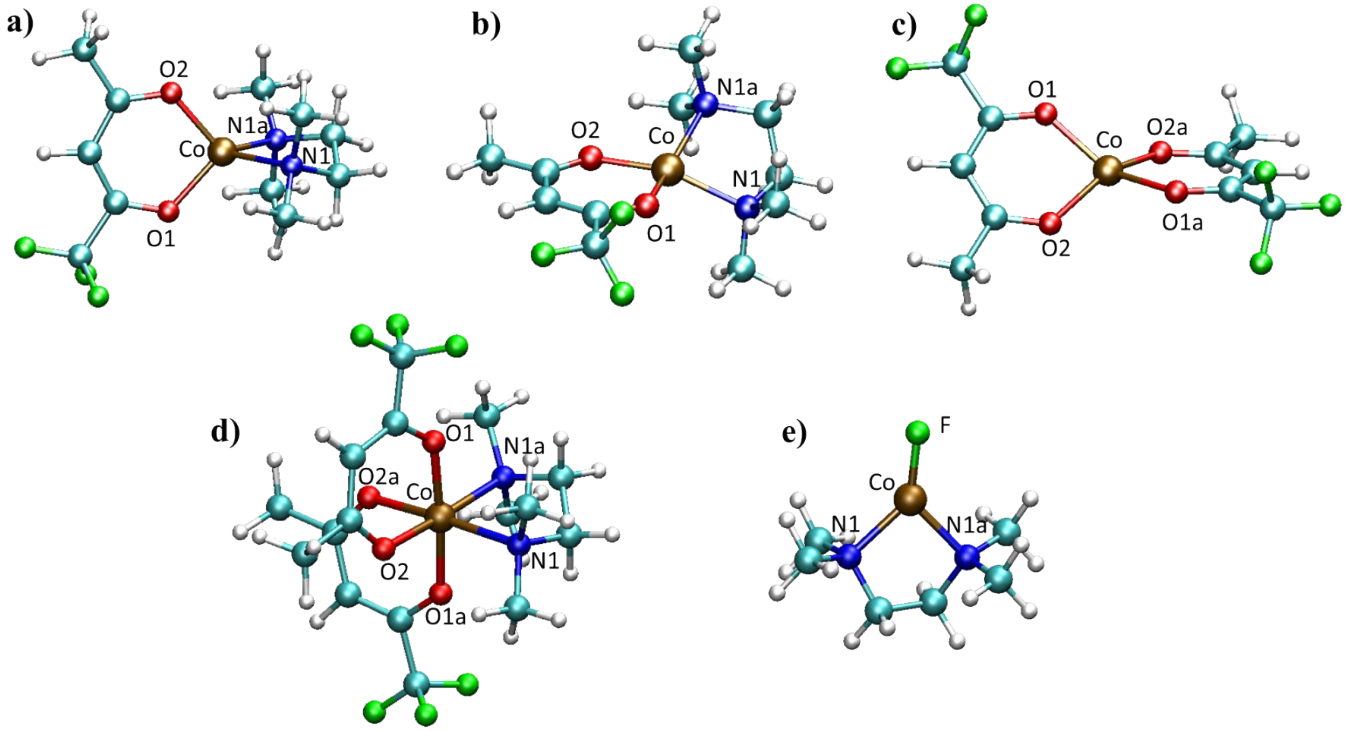

Figure S9. Graphical representation of the optimized structure of: (a) $Co(tfa)•TMEDA^+$, obtained by loss of a tfa^- ligand from $Co(tfa)_2$•TMEDA, minimum energy structure with a tetrahedral geometry; (b) $Co(tfa)•TMEDA^+$, distorted square geometry, 4.12 kcal×mol^{-1} higher in energy with respect to (a); (c) $Co(tfa)_2$, obtained by the loss of the neutral TMEDA ligand from $Co(tfa)_2$•TMEDA; (d) $[Co(tfa)_2•TMEDA]^{+•}$; (e) $[CoF(TMEDA)]^+$. Atom color codes: Co = brown; F = green; O = red; N = blue; C = cyan; H = white.

Besides the above-discussed fragments, we computed at the M06/D95+(d,p) level the optimized geometry of other ions formed in the ESI-MS experiments – namely, the distorted octahedral species $[Co(tfa)_2•TMEDA]^{+•}$ (Fig S9d) and the 3-coordinated moiety $[CoF(TMEDA)]^+$, exhibiting a nearly planar arrangement of Co, F, and nitrogen atoms (Fig. S9e). Relevant geometrical parameters of these ions are reported in Table S8. Both systems are characterized by metal-ligand distances shorter than in the parent compound - note in particular the drastic shortening of Co-O1/O1a bonds in $[Co(tfa)_2•TMEDA]^{+•}$.

System	Electronic energy (a.u.)	ZPE (a.u.)	ZPE-corrected energy (a.u.)	ZPE-corrected ΔE (kcal×mol^{-1})
$Co(tfa)_2$•TMEDA	-1779.062367	0.404878	-1778.657489	
$Co(tfa)_2$ distorted square	-1431.479602	0.180270	-1431.299332	
TMEDA	-347.510474	0.221087	-347.289388	
ΔE_1			0.068769	**+43.15**
Co(tfa)•$TMEDA^+$ tetrahedral	-1136.034311	0.315827	-1135.772873	
tfa^-	-642.816241	0.086334	-642.729907	
ΔE_2			0.154709	**+97.08**
Co(tfa)•$TMEDA^+$ tetrahedral	-1136.034311	0.315827	-1135.718484	
Co(tfa)•$TMEDA^+$ distorted square	-1136.027472	0.315561	-1135.711911	
$\Delta E_{(distorted\ square\ -\ tetrahedral)}$			0.006573	**+4.12**

Table S7. Energetics for the parent $Co(tfa)_2$•TMEDA complex and for the fragments pertaining to the decomposition routes 1) and 2). Electronic energies, ZPEs, and ZPE-corrected energies are in a.u. (hartree), while ZPE-corrected energy differences are in kcal×mol^{-1}.

	$Co(tfa)_2$•TMEDA	$[Co(tfa)_2$•TMEDA$]^{+\bullet}$	[Co(tfa)TMEDA]$^+$		$Co(tfa)_2$	[CoF(TMEDA)]$^+$
			Tetra	**Square**		
Length (Å)						
Co-O1	2.043	1.897	1.907	1.904	1.932	-
Co-O1a	2.043	1.897	-	-	1.932	-
Co-O2	2.064	2.032	1.911	1.910	1.931	-
Co-O2a	2.064	2.032	-	-	1.931	-
Co-N1	2.197	2.157	2.053	2.093	-	2.043
Co-N1a	2.197	2.157	2.057	2.087	-	2.043
Co-F	-	-	-	-	-	1.705
Angle (°)						
O1−Co−O1a	177.5	176.1	-	-	147.6	-
O1−Co−O2	88.0	86.9	98.2	90.7	89.5	-
N1−Co−N1a	83.4	84.3	88.4	83.7	89.5	88.3
O2-Co-O2a	90.1	86.9	-	-	148.5	-
O2-Co-N1	93.4	93.1	117.7	154.6	-	-
O1-Co-N1	93.5	94.9	118.1	97.1	-	-
N1-Co-F	-	-	-	-	-	135.9

Table S8. Relevant geometrical parameters for the optimized geometries of Co-containing ions and fragments: $[Co(tfa)_2$•TMEDA$]^{+\bullet}$ (Fig S9d, multiplicity: quintet); [Co(tfa)•TMEDA]$^+$ tetrahedral (Fig. S9a) and distorted square (Fig. S9b) (multiplicity: quartet); $Co(tfa)_2$ (Fig. S9c, multiplicity: quartet), [CoF(TMEDA)]$^+$ (Fig. S9e, multiplicity: quartet) at the M06/D95+(d,p) level of theory. $Co(tfa)_2$•TMEDA data at the same theory level are reported for comparison. Co pseudopotential/basis set of Ref.[24].

§ S5.4. Electronic excitation properties

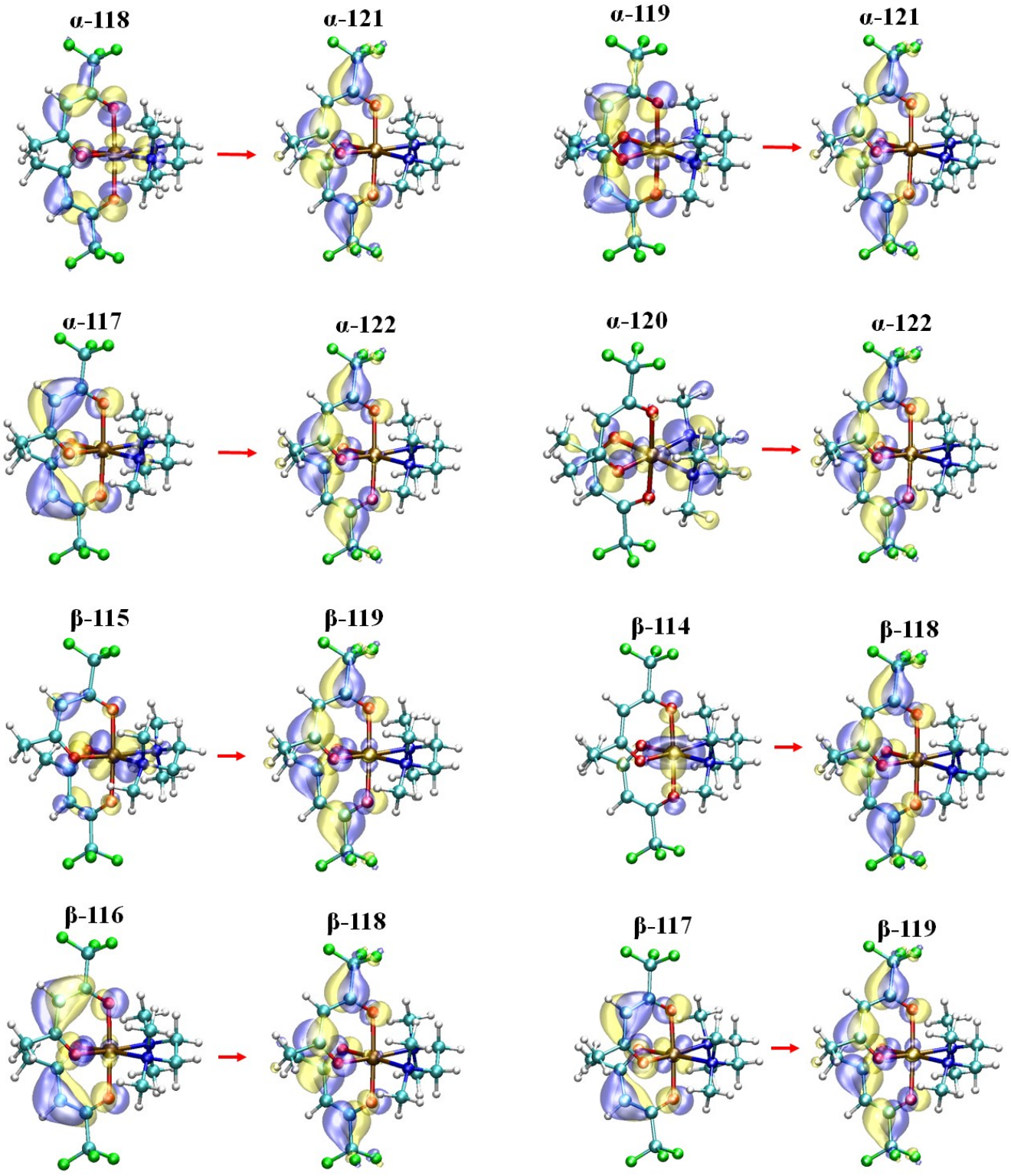

Figure S10. Graphical representation of the α-spin orbitals and β-spin orbitals involved in the main component of the electronic excitation spectrum, computed at λ = 264 nm (oscillator strength = 0.2238). The dominant contributions to the main peak are due to the excitations β-115 → β-119 (metal + ligand → ligand); α-118 → α-121 (ligand + metal → ligand), and β-116 → β-118 (mainly ligand → ligand π-π*). Atom colors: Co, brown; F, green; O, red; N, blue; C, cyan; H, white. Yellow and blue colors indicate positive (+0.03 *e*) and negative (-0.03 *e*) isosurfaces of the spin orbitals, respectively.

Electronic structure analysis enables to obtain insight on the nature of the electronic transitions pertaining to $Co(tfa)_2$•TMEDA. The molecular α- and β-spin orbitals involved in the electronic excitation components of the most intense transition (computed at λ = 264 nm, with 0.2238 oscillator strength) are shown in Fig. S10. As a general feature, we notice that the final states (α-121, α-122, β-118, β-119, respectively) are mostly localized on the tfa ligands, and are formed by combinations of the tfa π* states. Conversely, the initial states of the electronic excitation components are generally characterized by an appreciable degree of admixing between ligand and Co-d states. As a matter of fact, some of the involved spin orbitals are spread on both Co and ligands (see *e.g.* α-118, α-119, α-120, and β-117 in Fig. S10). On the other hand, β-115 and β-114 essentially belong to the metal center, with very few contributions from tfa. Finally, β-116 and α-117 are mostly localized on tfa ligands and have a dominant π-character.

The excitations that mainly contribute to the λ = 264 nm transition are the β-115 → β-119, α-118 → α-121, β-116 → β-118 ones. From Fig. S10, it can be seen that these three excitations have a metal (dominant) + ligand → ligand (M + L → L), ligand (dominant) + metal → ligand (L + M→ L), and ligand-ligand (L → L) nature, respectively. Taken together, these results enable to conclude that the most intense absorption of the UV spectrum has a mixed M + L → L character.

As mentioned in the main text, inspection of the TDDFT excitations revealed the presence of two very weak transitions (oscillator strength = 0.0001) at 578 and 524 nm, respectively (Fig 3b). As both excitations essentially involve the 3d orbitals of Co, they can therefore be denoted as metal-to-metal (M → M) transitions. For sake of completeness, the TDDFT calculations also predicted two very weak excitations (oscillator strength = 0.0001) in the IR region (2128 and 1710 nm), which have M → M character as well. Indeed, the occurrence of weak M → M absorption bands in the visible and IR region in electronic spectra of Co(II) octahedral complexes is well documented in the literature.[9, 27, 28]

The two weak transitions in the visible range (578 and 524 nm) - not clearly distinguishable in the experimental UV-vis spectrum in dilute solution (Fig 3a), may be responsible of the red-orange color of the $Co(tfa)_2$•TMEDA crystal. To support this hypothesis, we investigated the electronic structure of the $Co(tfa)_2$•TMEDA crystal, as discussed in the next section.

§ S5.5. Electronic structure of the $Co(tfa)_2$•TMEDA crystal

The band structure of the $Co(tfa)_2$•TMEDA crystal was calculated, using the X-ray coordinates and cell parameters, with the QE code by adopting the previously described computational setup for the periodic electronic structure calculations (see § S5.1), and performing a K-point sampling on a 2×1×1 mesh. For comparison, a QE calculation with the same DFT-U parameters was also performed on the monomer, using the X-ray coordinates, in a cubic box of 20 Å.

The total magnetization of the crystal was determined by calculating the energy of the different possible arrangements of spin states of the four Co centers in the unit cell. The antiferromagnetic arrangement (total magnetization = 0, absolute magnetization = 12) resulted energetically favored with respect to the ferromagnetic arrangement (total and absolute magnetization = 12) by 9.6 kcal×mol^{-1}. A graphical representation of the $Co(tfa)_2$•TMEDA crystal highlighting the antiferromagnetic arrangement of the metal centers is shown in Fig. S11.

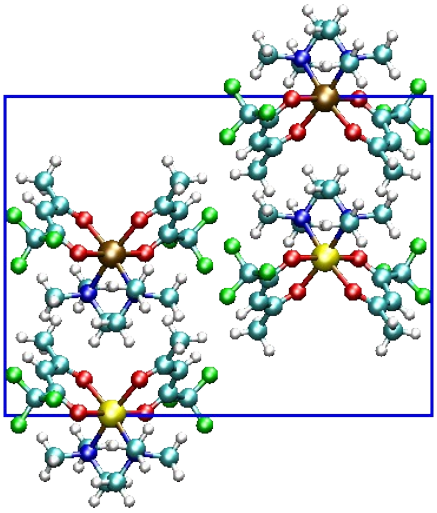

Figure S11. Graphical representation of the unit cell of the $Co(tfa)_2$•TMEDA crystal projected in the *bc* plane, evidencing the antiferromagnetic arrangement of the Co centers. Atom colors: Co, spin-up: brown; Co, spin-down: yellow; F, green; O, red; N, blue; C, cyan; H, white. The unit cell is indicated by blue solid lines.

The electronic structure calculation of the crystal predicted a band gap of 2.35 eV (λ=528 nm), hence in keeping with the excitation wavelengths predicted in that spectral region by the TDDFT calculations (578 and 524 nm, see section § S5.4). Such a value, corresponding to green-light absorption, is also in line with the red-orange color exhibited by the $Co(tfa)_2$•TMEDA crystal (see Fig. 1, main text).

Inspection of the density of states (DOS) and of the projected density of states (PDOS) calculated for the $Co(tfa)_2$•TMEDA crystal evidenced that the highest occupied states and the lowest unoccupied states are constituted by Co 3d orbitals. As can be seen in Fig. S12, the Co-3d PDOS of the crystal for the lowest empty states (peaks at 2.3-2.5 eV) has a moderate magnitude, while the Co-3d PDOS of the monomer

for the lowest empty states (the feature at ≈2.75 eV) has a much smaller value. This comparison among the Co-3d PDOS suggests therefore that the M → M transition intensity for $Co(tfa)_2$•TMEDA should drastically decrease in passing from the crystal to the monomer form. Hence, the intensity of these features might be so weak to be indistinguishable from the background in the experimental UV-vis spectrum of the complex in ethanol solution.

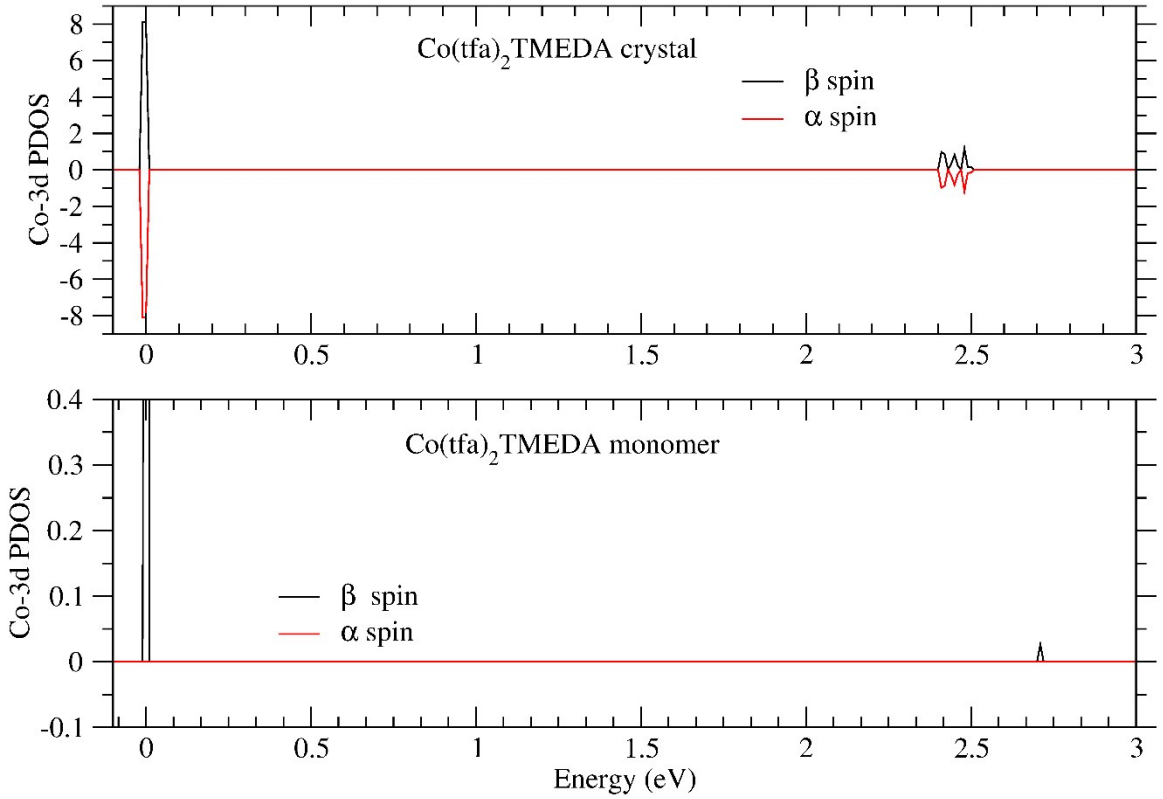

Figure S12. Projected density of states (PDOS) of Co-3d states for the $Co(tfa)_2$•TMEDA crystal and for the monomer. In both cases, the energy of the highest occupied states has been taken as a reference and set to zero to facilitate comparison among crystal and monomer PDOS. Note the different scale of crystal *vs*. monomer PDOS: the PDOS for the monomer has been magnified to better visualize the feature at 2.75 eV, corresponding to the Co 3d empty states.

§ S6. Chemico-physical characterization of cobalt oxide films

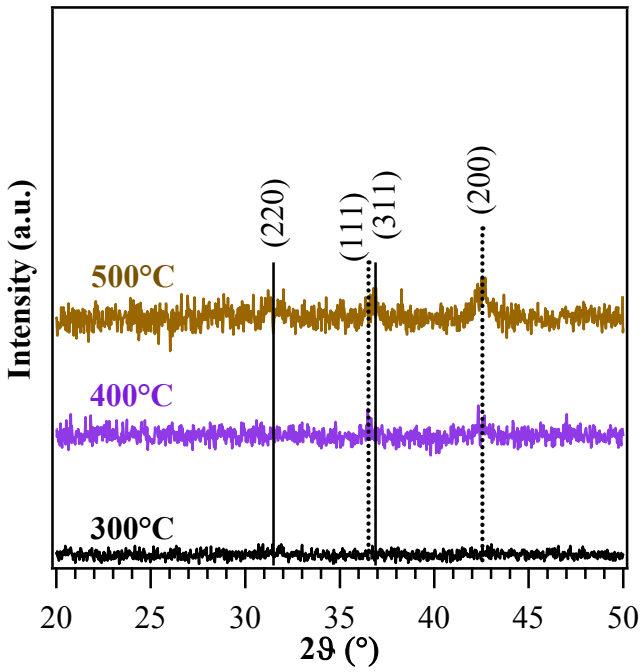

Figure S13. XRD patterns of cobalt oxide films grown on Si(100) under a dry O_2 atmosphere. The reference peak positions for CoO[29] and Co_3O_4[30] are marked by dashed and continuous vertical lines, respectively.

Preliminary XRD analyses on samples obtained under a dry O_2 atmosphere (Fig. S13) did not show any appreciable diffraction peak for a growth temperature of 300°C, in line with previous results obtained in the CVD of cobalt oxides from $Co(hfa)_2$•TMEDA.[31] In a different way, the specimen obtained at 400°C was characterized by the presence of peaks at 2ϑ = 36.6° and 42.4°, related to (111) and (200) crystallographic planes of cubic CoO.[29] For the former, a concurrent contribution of the (311) peak from spinel-type cubic Co_3O_4[30] (2ϑ = 36.8°) could not be unambiguously excluded, due to the signal low intensity and rather large peak width. An increase of the growth temperature to 500°C resulted in an intensity increase of the above signals, along with the appearance of a peak at 2ϑ = 31.5° due to the (220) Co_3O_4 reflection.[30] In line with previously reported results,[31-34] these data indicated that an increase in the growth temperature favored the formation of Co_3O_4 over CoO.

The patterns in Fig. S13 showed a limited number of broad and very weak diffraction peaks, indicating the occurrence of small nanoaggregates (whose dimensions were estimated to be ≈10 nm) with a low crystallinity degree.

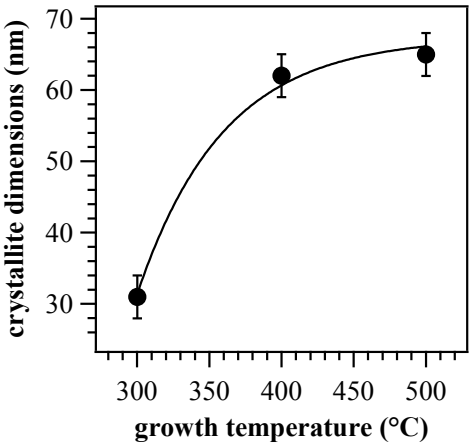

Figure S14. Dependence of the average crystallite size on the growth temperature for specimens obtained under a wet O_2 atmosphere.

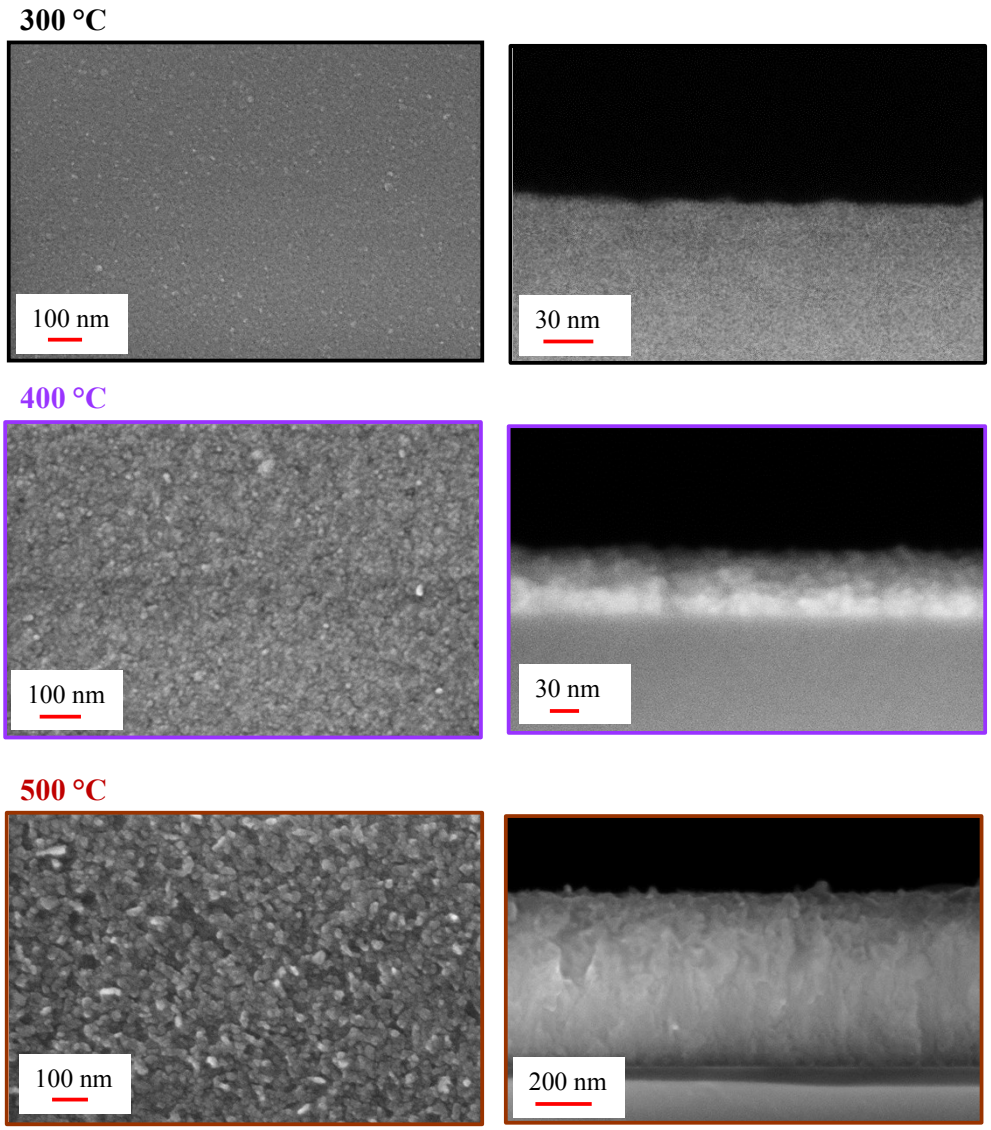

Figure S15. Representative plane-view and cross-sectional FE-SEM images of cobalt oxide films deposited under a dry O_2 atmosphere at 300, 400 and 500°C.

FE-SEM images of specimens grown in a dry O_2 atmosphere (Fig. S15) displayed the formation of rather compact multi-granular films, whose thickness increased with the adopted deposition temperature (10, 80 and 550 nm at 300, 400 and 500°C, respectively).

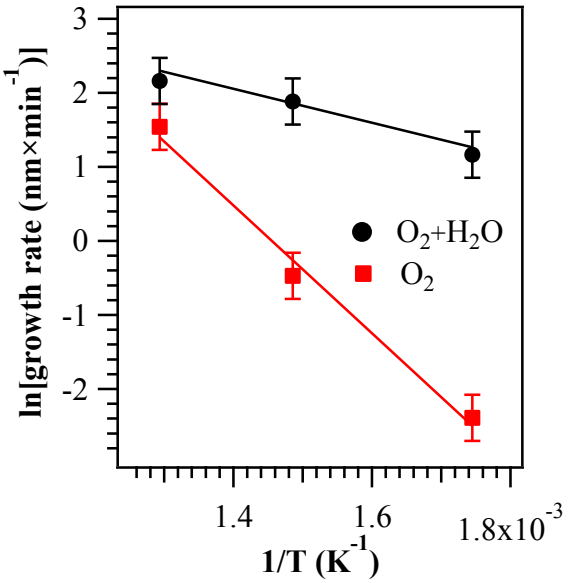

Figure S16. Arrhenius plot of the growth rates[35] as a function of substrate temperature for cobalt oxide films grown under dry and wet O_2 atmospheres. In both cases, a surface-reaction-limited regime occurred, although the curve slope was appreciably steeper under dry O_2.

Growth rate values were calculated as the ratios between the specimen thickness determined by FE-SEM and the deposition time (120 min for all the samples). At 500°C in wet atmosphere, a growth rate of ≈9 nm×min^{-1} was obtained, a value in line with previous results for the CVD of cobalt oxides from dicarbonyl cyclopentadienyl cobalt,[32] $Co(dpm)_2$ (dpm = 2,2,6,6-tetramethyl-3,5-heptanedionate),[33] $Co(hfa)_2$•TMEDA[31] and *bis*(4-(isopropylamino)-pent-3-en-2-onato)cobalt(II)[36] under analogous conditions. Compared with $Co(acac)_3$ (acac = 2,4-pentanedionate),[37, 38] $Co(hfa)_2$•$2H_2O$•X (X= diglyme, triglyme and tetraglyme)[39, 40] and with $Co(hfa)_2$•$2H_2O$,[41] the present $Co(tfa)_2$•TMEDA precursor yielded higher growth rates for the resulting Co_3O_4 films.

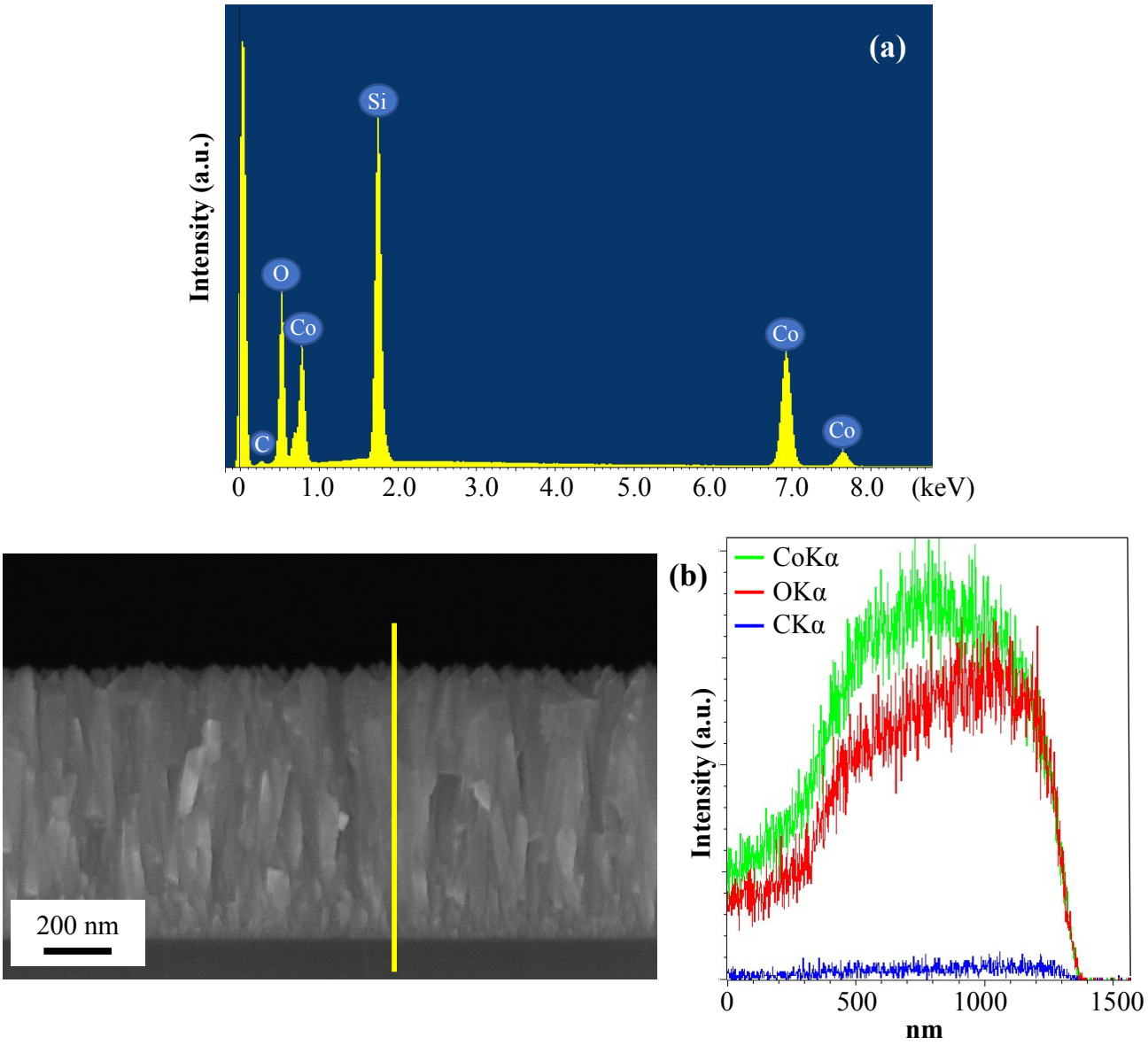

Figure S17. EDXS spectrum (a) and cross-sectional line scan data (b), recorded along the yellow line marked in cross-sectional FE-SEM image, for a Co_3O_4 film deposited at 400°C under a wet O_2 atmosphere.

§ S.7 References

1 *SAINT*, Version 8.38A, Bruker AXS Inc., Madison, Wisconsin, USA, 2017.

2 *SADABS*, Version 2016/2, Bruker AXS Inc., Madison, Wisconsin, USA, 2016., *SADABS*, Version 2016/2, Bruker AXS Inc., Madison, Wisconsin, USA, 2016.

3 G. M. Sheldrick, *Acta Cryst.*, 2015, **A71**, 3-8.

4 *International Tables for Crystallography, Vol. C* (Ed.: A. J. Wilson), Kluwer Academic Publishers, Dordrecht, The Netherlands, **1992**, Tables 6.1.1.4 (pp. 500–502), 4.2.6.8 (pp. 219–222), and 4.2.4.2 (pp. 193–199).

5 A. L. Spek, *Acta Cryst.*, 2009, **D65**, 148-155.

6 I. Bertini, L. Messori, G. Golub, H. Cohen and D. Meyerstein, *Inorg. Chim. Acta*, 1995, **235**, 5-8.

7 https://cccbdb.nist.gov/vibscalejust.asp.

8 R. D. Johnson III, *NIST Computational Chemistry Comparison and Benchmark Database*, version 21; August 2020, NIST Standard Reference Database N°101.

9 G. Bandoli, D. Barreca, A. Gasparotto, C. Maccato, R. Seraglia, E. Tondello, A. Devi, R. A. Fischer and M. Winter, *Inorg. Chem.*, 2009, **48**, 82-89.

10 A. Gasparotto, D. Barreca, A. Devi, R. Fischer, E. Fois, A. Gamba, C. Maccato, R. Seraglia, G. Tabacchi and E. Tondello, *ECS Trans.*, 2009, **25**, 549-556.

11 D. Barreca, G. Carraro, A. Gasparotto, C. Maccato, R. Seraglia and G. Tabacchi, *Inorg. Chim. Acta*, 2012, **380**, 161-166.

12 G. Tabacchi, E. Fois, D. Barreca and A. Gasparotto, *Phys. Status Solidi A*, 2014, **211**, 251-259.

13 G. Bandoli, D. Barreca, A. Gasparotto, R. Seraglia, E. Tondello, A. Devi, R. A. Fischer, M. Winter, E. Fois, A. Gamba and G. Tabacchi, *Phys. Chem. Chem. Phys.*, 2009, **11**, 5998-6007.

14 D. Barreca, G. Carraro, E. Fois, A. Gasparotto, F. Gri, R. Seraglia, M. Wilken, A. Venzo, A. Devi, G. Tabacchi and C. Maccato, *J. Phys. Chem. C*, 2018, **122**, 1367-1375.

15 P. Giannozzi, S. Baroni, N. Bonini, M. Calandra, R. Car, C. Cavazzoni, D. Ceresoli, G. L. Chiarotti, M. Cococcioni, I. Dabo, A. Dal Corso, S. de Gironcoli, S. Fabris, G. Fratesi, R. Gebauer, U. Gerstmann, C. Gougoussis, A. Kokalj, M. Lazzeri, L. Martin-Samos, N. Marzari, F. Mauri, R. Mazzarello, S. Paolini, A. Pasquarello, L. Paulatto, C. Sbraccia, S. Scandolo, G. Sclauzero, A. P. Seitsonen, A. Smogunov, P. Umari and R. M. Wentzcovitch, *J. Phys.: Condens. Matter*, 2009, **21**, 395502.

16 J. P. Perdew, K. Burke and M. Ernzerhof, *Phys. Rev. Lett.*, 1996, **77**, 3865-3868.

17 S. Grimme, *J. Comput. Chem.*, 2006, **27**, 1787-1799.

18 M. Cococcioni and S. de Gironcoli, *Phys. Rev. B*, 2005, **71**, 035105.

19 M. J. Frisch, G. W. Trucks, H. B. Schlegel, G. E. Scuseria, M. A. Robb, J. R. Cheeseman, G. Scalmani, V. Barone, B. Mennucci, G. A. Petersson, H. Nakatsuji, M. Caricato, X. Li, H. P. Hratchian, A. F. Izmaylov, J. Bloino, G. Zheng, J. L. Sonnenberg, M. Hada, M. Ehara, K. Toyota, R. Fukuda, J. Hasegawa, M. Ishida, T. Nakajima, Y. Honda, O. Kitao, H. Nakai, T. Vreven, J. A. Montgomery, Jr., J. E. Peralta, F. Ogliaro, M. Bearpark, J. J. Heyd, E. Brothers, K. N. Kudin, V. N. Staroverov, T. Keith, R. Kobayashi, J. Normand, K. Raghavachari, A. Rendell, J. C. Burant, S. S. Iyengar, J. Tomasi, M. Cossi, N. Rega, J. M. Millam, M. Klene, J. E. Knox, J. B. Cross, V. Bakken, C. Adamo, J. Jaramillo, R. Gomperts, R. E. Stratmann, O. Yazyev, A. J. Austin, R. Cammi, C. Pomelli, J. W. Ochterski, R. L. Martin, K. Morokuma, V. G. Zakrzewski, G. A. Voth, P. Salvador, J. J. Dannenberg, S. Dapprich, A. D. Daniels, O. Farkas, J. B. Foresman, J. V. Ortiz, J. Cioslowski, and D. J. Fox, GAUSSIAN 09 (Revision B.01), Gaussian, Inc., Wallingford CT, 2010.

20 Y. Zhao and D. G. Truhlar, *Theor. Chem. Acc.*, 2008, **120**, 215-241.

21 J.-D. Chai and M. Head-Gordon, *Phys. Chem. Chem. Phys.*, 2008, **10**, 6615-6620.

22 T. H. Dunning, Jr., P. J. Hay in *Modern Theoretical Chemistry, Vol. 2, Chap. 1*, Plenum, New York, 1976.

23 W. Humphrey, A. Dalke and K. Schulten, *J. Mol. Graphics*, 1996, **14**, 33-38.

24 A. Bergner, M. Dolg, W. Küchle, H. Stoll and H. Preuß, *Mol. Phys.*, 1993, **80**, 1431-1441.

25 A. E. Reed, L. A. Curtiss and F. Weinhold, *Chem. Rev.*, 1988, **88**, 899-926.

26 E. D. Glendening, J. K. Badenhoop, A. E. Reed, J. E. Carpenter, J. A. Bohmann, C. M. Morales and F. Weinhold, *NBO 5.0, Theoretical Chemistry Institute, University of Wisconsin, Madison, USA*, 2001.

27 L. C. Tzavellas, C. Tsiamis, C. A. Kavounis and C. J. Cardin, *Inorg. Chim. Acta*, 1997, **262**, 53-59.

28 A. Bencini, C. Benelli, D. Gatteschi and C. Zanchini, *Inorg. Chem.*, 1983, **22**, 2123-2126.

29 Pattern N° 43-1004, JCPDS (2000).

30 Pattern N° 42-1467, JCPDS (2000).

31 D. Barreca, A. Gasparotto, O. I. Lebedev, C. Maccato, A. Pozza, E. Tondello, S. Turner and G. Van Tendeloo, *CrystEngComm*, 2010, **12**, 2185-2197.

32 S. Schmid, R. Hausbrand and W. Jaegermann, *Thin Solid Films*, 2014, **567**, 8-13.

33 D. Barreca, C. Massignan, S. Daolio, M. Fabrizio, C. Piccirillo, L. Armelao and E. Tondello, *Chem. Mater.*, 2001, **13**, 588-593.

34 M. Melzer, C. K. Nichenametla, C. Georgi, H. Lang and S. E. Schulz, *RSC Adv.*, 2017, **7**, 50269-50278.

35 A. C. Jones and M. L. Hitchman, *Chemical Vapor Deposition: Precursors, Processes and Applications*, Royal Society of Chemistry, Cambridge, UK, 2009.

36 K. J. Puring, D. Zywitzki, D. H. Taffa, D. Rogalla, M. Winter, M. Wark and A. Devi, *Inorg. Chem.*, 2018, **57**, 5133-5144.

37 P. Mountapmbeme Kouotou and Z.-Y. Tian, *Surf. Coat. Technol.*, 2017, **326**, 11-17.

38 P. M. Kouotou, Z.-Y. Tian, U. Mundloch, N. Bahlawane and K. Kohse-Höinghaus, *RSC Adv.*, 2012, **2**, 10809-10812.

39 A. Gulino and I. Fragalà, *Inorg. Chim. Acta*, 2005, **358**, 4466-4472.

40 A. Gulino, P. Dapporto, P. Rossi and I. Fragalà, *Chem. Mater.*, 2003, **15**, 3748-3752.

41 A. Gulino, G. Fiorito and I. Fragalà, *J. Mater. Chem.*, 2003, **13**, 861-865.